Reconfigurable nanophotonic silicon probes for sub-millisecond deep-brain optical stimulation

Aseema Mohanty[1,2,7], Qian Li [ID][3,4,7], Mohammad Amin Tadayon[1], Samantha P. Roberts[1], Gaurang R. Bhatt [ID][1], Euijae Shim[1], Xingchen Ji [ID][1,2], Jaime Cardenas [ID][1,5], Steven A. Miller[1], Adam Kepecs [ID][3,4,6] ✉ and Michal Lipson [ID][1] ✉

[1]Department of Electrical Engineering, Columbia University, New York, NY, USA. [2]School of Electrical and Computer Engineering, Cornell University, Ithaca, NY, USA. [3]Cold Spring Harbor Laboratory, Cold Spring Harbor, New York, NY, USA. [4]Department of Neuroscience, Washington University in St. Louis, St. Louis, MO, USA. [5]Institute of Optics, University of Rochester, Rochester, NY, USA. [6]Department of Psychiatry, Washington University in St. Louis, St. Louis, MO, USA. [7]These authors contributed equally: Aseema Mohanty, Qian Li. ✉e-mail: akepecs@wustl.edu; ml3745@columbia.edu

Contents

Supplementary Discussion 1: Optical crosstalk and loss within the nanophotonic probe

The 1x2 switch shows a high ON/OFF contrast switching behavior of 17 dB or 50:1, which is well above the dynamic range that is necessary for optogenetics considering the neural activation threshold. However, there is a higher level of optical crosstalk within the 1x8 switching network due to fabrication variations across the switches that cannot be actively compensated as seen in Figure 3 and Supplementary Movie 1. Supplementary 9 shows a 2D color map showing the whole 1x8 switch crosstalk performance when the 8 beams are individually turned on. Note that having only one emitter turned ON is the worst case scenario since it requires the most number of switches to have perfect destructive interference (i.e. OFF). Since, the neurons have a threshold for activation of about 10 mW/mm^2, in our in-vivo experiment (see Fig. 4), we were able to optimize the laser power, so that all combinations of activation of three neurons and optical crosstalk was not an issue. One can see from Supplementary Figure 9 that the average ON/OFF contrast is 13 dB, i.e. a contrast ratio of about 20:1. The beam 1 configuration has a slightly higher cross talk due to a fabrication error leading to a smaller average ON/OFF contrast of 7 dB, i.e. about 5:1, which is still above the needed contrast for optogenetic activation. Although 50:1 ON/OFF contrast is sufficient for many applications, as channel counts increase and for more sensitive applications this optical crosstalk can be improved. To address the issue at the device level, we can design more fabrication robust Mach-Zehnder interferometer (MZI) switches by increasing the tolerances of 2x2 (MMI) splitters and decreasing the lengths and increasing the widths of the MZI arms to reduce residual phase errors accumulated within the arms[1,2]. To address the issue at a system level, there are different MZI architectures that reduce optical crosstalk by creating blocking states[3].

The primary optical losses within the structure are due to coupling between the fiber and the chip and propagation losses through the waveguides. For coupling losses, in this preliminary demonstration since there was sufficient light output for neural activation, we did not incorporate a spot size converter leading to a coupling loss of about 16 dB due to the mode mismatch between the fiber and the input waveguide. This loss could be reduced as low as 0.5 dB by optimizing the design of the waveguide and using a spot size converter[4–7]. Similarly, our propagation losses of approximately 1.5 dB/mm were higher than expected but sufficiently low to enable neural activation for our 8-beam probe. Note that waveguides with losses down to 0.1-0.3 dB/mm have been demonstrated for blue wavelengths by optimizing the geometry[8,9] and fabrication processing steps[10].

Supplementary Discussion 2: Thermal management of the nanophotonic switching network

In order to characterize the thermal crosstalk, we measured the temperature rise of one of the switches on the probe, as we turn on a neighboring switch for various duty cycles at 200 Hz (see Supplementary Figure 10a). We measured a temperature change of less than 1°C for less than 40% duty cycle pulsing, corresponding to a $< \pi/25$ radian phase shift which has a negligible effect on the switch performance. We extracted the temperature rise by probing the change in resistance of the Pt wire and calibrated the temperature coefficient of resistance of Pt by measuring the change in resistance of multiple switches as a function of temperature in a vacuum probe station with a temperature stabilized heated chuck (see Methods). We confirm this measurement using a thermal imaging camera that provides a spatial temperature distribution

across the probe when a single switch (S1) is turned on (see Supplementary Figure 10b-d). Within less than 130 μm, the temperature distribution is flat preventing a significant phase difference between neighbouring interferometric switch's arms. As shown in Supplementary Figure 10e, thermal crosstalk from a neighbouring switch has negligible effect on a switch's performance. The maximum background temperature the system can withstand is not limited by the photonics but the maximum temperature the brain can handle at the tip of the probe. **Note:** the thermal imaging camera has a limited resolution of greater than 20 μm, which does not accurately capture the absolute temperature distribution immediately near the microheater, about 30°C. However, this method provides a qualitative behaviour for the temperature distribution at the millimetre scale.

In order to estimate the effect of the switches on the brain temperature, we measure a rise in temperature of approximately 0.2-0.4°C at the tip of the probe for the duty cycles (10-20%) and frequencies used in this work (see Supplementary Figure 10d). This temperature is an upper limit on the rise in temperature of the surrounding brain tissue and already well below the safe operating conditions (< 2°C)[11]. The worst case switch configuration in terms of heat for this 1x8 switch for the current probe design is when the 4 switches at the bottom of the binary tree are fully on and the rest of the switches are half on. This will lead to a temperature increase at the tip of the probe to be 1.1°C for 10% duty cycle. The average temperature increase for generating all (2^8 or 256) patterns is 0.55°C.

Because microheaters are positioned outside of the brain, temperature increases can be substantially lowered using active thermal management. Using heat sinks and optimized probe and microheater designs will enable further scaling of the number of emitters. For example, using a standard heat sink with 15°C/W thermal resistance, one can generate 2^{64}, or 1.8×10^{19}, different patterns (using 64 emitters) with 20% duty cycle and 200 Hz pulsing while maintaining a change of no more than 1°C at the tip of the probe that is inserted. The temperature rise at the tip of the probe can also be reduced by simply increasing the distance between the switches and the emitters, increasing the area of the base of the probe, and thinning the shank of the probe further. In addition, the microheater design can be improved to further decrease the power dissipation by at least a factor of 10 by increasing the light interaction with the heat, for example, by coiling the waveguide under the heater and creating thermal isolation trenches[12]. Recently, a low power microheater based visible phase shifter was demonstrated with an order of magnitude less power for a π phase shift using a microresonator structure[13]. This would enable 10x more switches without a heat sink.

Supplementary Discussion 3: Minimizing footprint of the nanophotonic probe

To minimize the amount of tissue damage, the footprint of the inserted part of probe should be reduced. Our platform is fully compatible with fabrication processes used for previous nanophotonic probe demonstrations which have probe thicknesses down to 20 μm and widths near 50 μm[8,14]. In principle, the minimum theoretical spacing between emitters is on the order of 20% the wavelength, about 100 nm in our case, enabling more than a 1000 cell-sized emitters along a 4 cm long probe.

We show an alternative grating emitter and electrode arrangement to what we have shown in this work to reduce the width of the probe with increasing number of emitters (see Supplementary Figure 11). The width of the probe is primarily determined by how closely the routing waveguides can be spaced. The minimum waveguide spacing depends on the evanescent coupling strength between the waveguides, which is determined by the waveguide geometry. Here we use a conservative estimate of waveguides with a 1 μm width and 500 nm gap. Using the shortened grating structure as shown in previous work, for 8 channels, this reduces the width to about 60 μm[8]. For 64 channels, this would be about 150 μm. However, to truly scale up these probes to potentially 1000's of emitters, optical multiplexing and beam shaping and steering techniques should be employed.
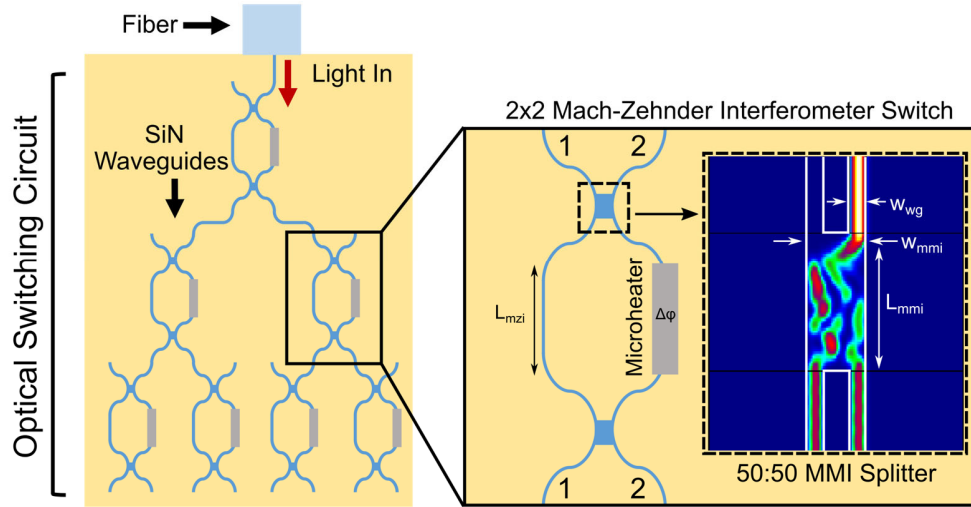
Supplementary Figure 1. Thermo-optic switch design. The thermo-optic switch is based on a Mach-Zehnder Interferometer (MZI) created using SiN waveguides and a Pt microheater. The light comes into the MZI into either arm with the same phase, the light is split equally at a 50:50 splitter, the light travels through both arms for the same length, and the light is split equally again with a 50:50 splitter. One of the arms has a microheater aligned on top, so as the power on the heater is increased, the refractive index of the waveguide in that arm is increased due to the thermo-optic effect. The change in refractive index leads to a phase difference ($\Delta\varphi$) between the two arms, which allows the continuous control of light between the two arms. Where $\Delta\varphi$ is proportional to the change in index and L_{mzi}. For the splitter we use a multimode interferometer (MMI), with a length (L_{mmi}) of 12.6 μm and width (w_{mmi}) of 1.2 μm. An MMI uses higher order modes and the self-imaging principle to create fabrication tolerant, compact, and fairly polarization insensitive structures for splitting light. The inset shows a numerical simulation (Eigenmode Expansion Method, FIMMWAVE software) of the normalized intensity of the light when light is input through port 2. The structure behaves identically, if light is input through the port 1 instead.

Si₃N₄   **SiO₂**   **SU-8**

Si   **Pt/Al**   **Pt/Al**

1) Deposit low pressure chemical vapor silicon nitride on oxidized silicon wafer.

2) Pattern and etch silicon nitride waveguides.

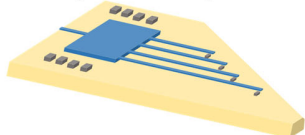3) Deposit low pressure chemical vapor silicon dioxide.

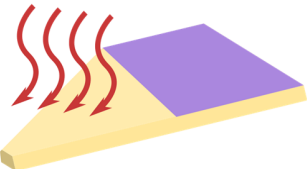4) Sputter deposit and pattern switches, wires, and recording sites using lift-off.

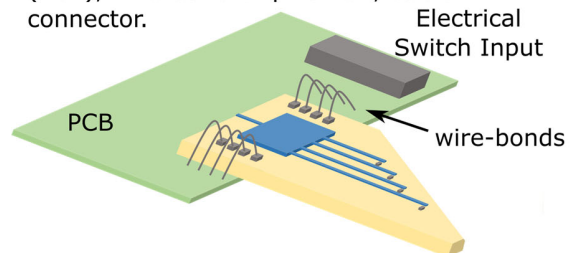5) Pattern SU-8 for selective insulation.
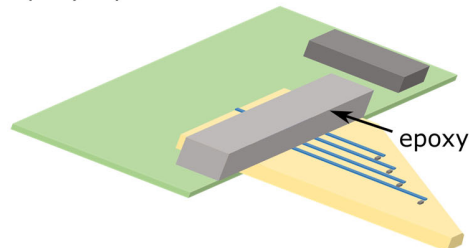
6) Dice chips to form probe.

7) Cover the base of the backside of the chip with a protective polymer and etch the backside silicon substrate.

8) Mount chip on Printed Circuit Board (PCB), wire-bond chip to PCB, solder connector.

Electrical Switch Input

PCB

wire-bonds
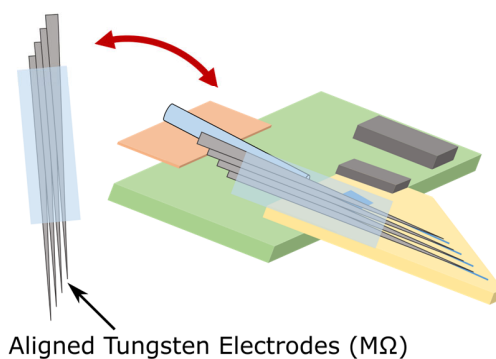
9) Cover wire-bonds with protective epoxy layer.

epoxy

10) Actively align and attach pre-assembled fiber using UV-cure adhesive.

Fiber-mounted on substrate
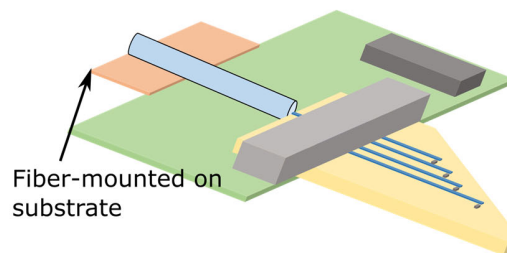
For discrete electrode version: Attach pre-aligned electrodes on top of chip.

Aligned Tungsten Electrodes (MΩ)

Supplementary Figure 2. Fabrication and packaging process of the nanophotonic probe.
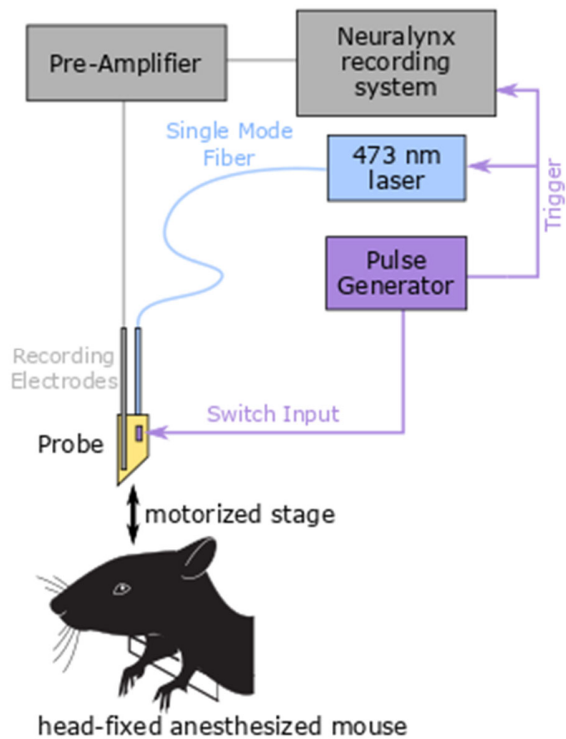
Supplementary Figure 3. Experimental setup for in-vivo demonstration. The anesthetized mouse is placed onto the stereotaxic apparatus. A pulse generator (Pulse Pal) was used to send 7 timed voltage patterns to the 7 nanophotonic switches and 1 synchronized TTL output to trigger laser pulses. A Neuralynx Digital Lynx system was used to acquire the pre-amplified 8-channel neural activities. This system also included a digital input channel to acquire laser pulses sequence for synchronization of the light stimulus and neural spikes.
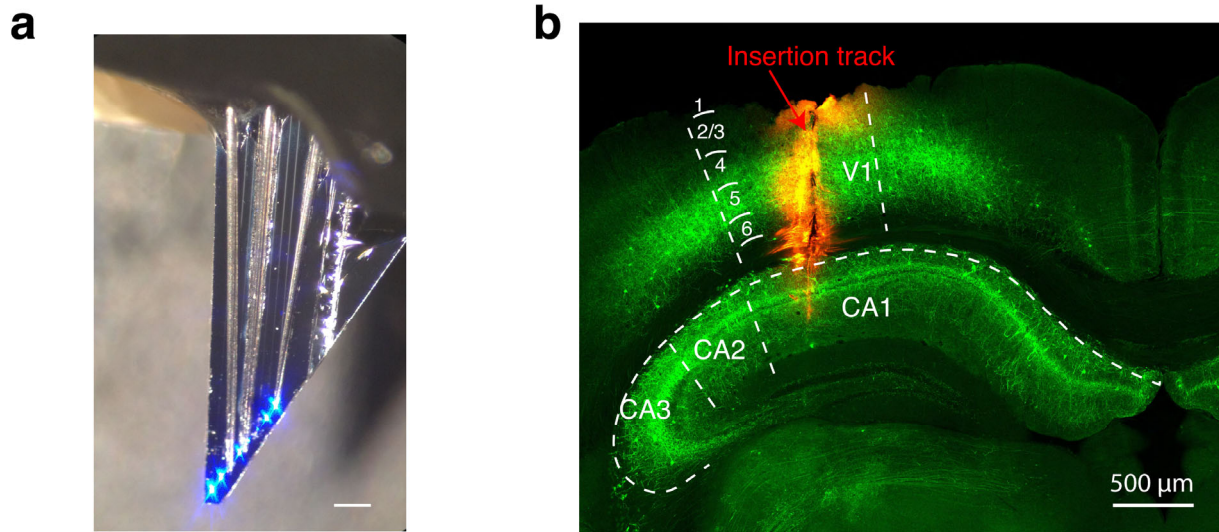
Supplementary Figure 4. Electrode arrangement and switching configuration for in-vivo experiment in Figure 4. a) Shows a microscope image of the electrode arrangement of the device used in the in-vivo demonstration. Here we use three stereotrodes (pre-assembled pairs of tungsten electrodes) aligned to beam 1, beam 2, and beam 3 as shown in Figure 4a (scale bar is 250 µm). b) Histological section of the brain depicts the insertion track (coated with a dye (DiL) in red) across the layer 2-6 visual cortex (V1) and hippocampus (CA1), with the deepest site reaching ~1300 µm from the brain surface. ChETA-eYFP expressing in the Gad2 interneuron is shown in green.
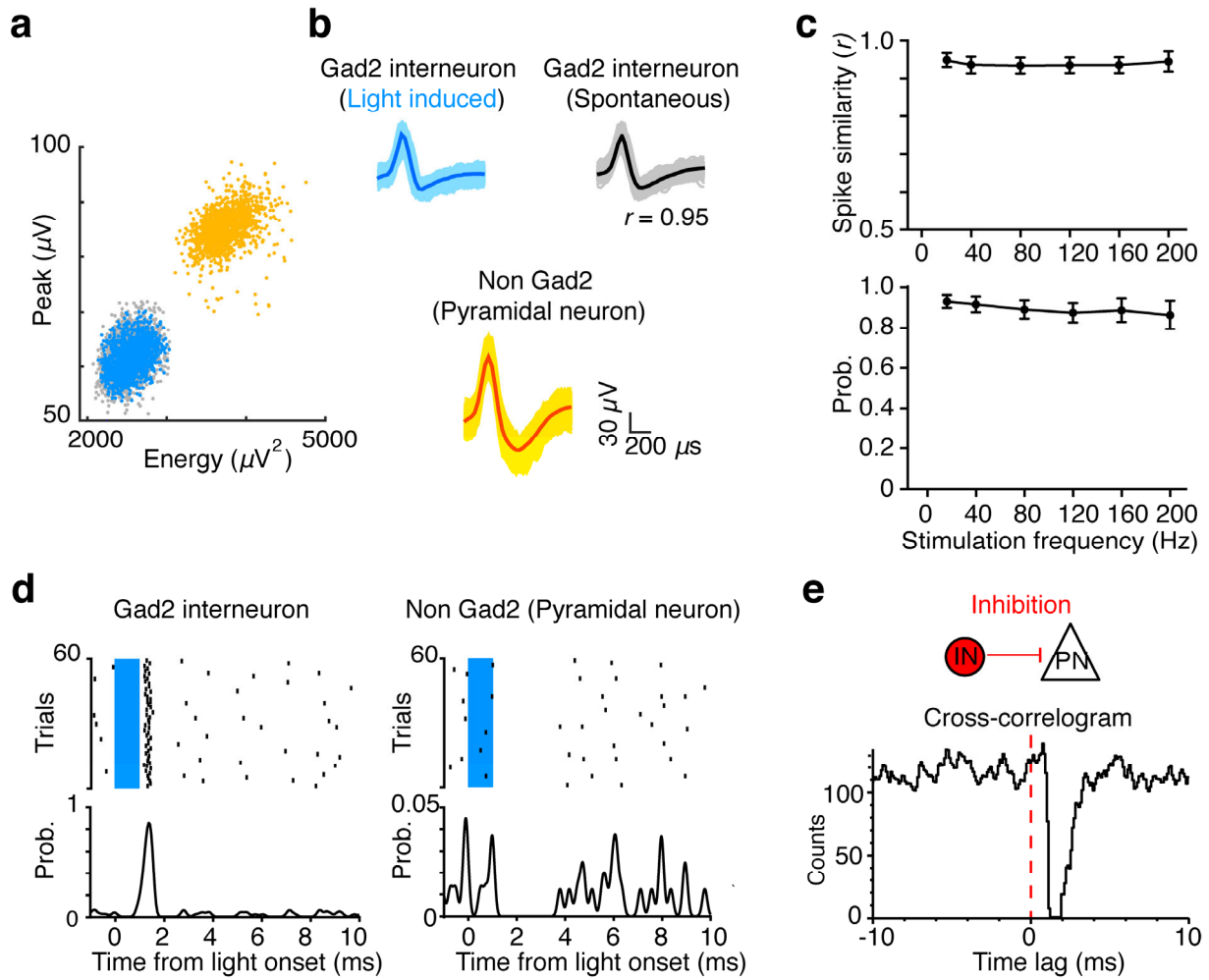
Supplementary Figure 5. Identification of ChETA-expressing Gad2 interneuron by light tagging test. a) Spike sorting example. Two individual neuron clusters, recorded from the same recording electrode, are classified based on the property of spike waveform (energy and peak). ChETA-expressing Gad2 interneuron exhibits light-induced spikes (superimposed in blue dots), which are overlaid with the spontaneous spikes (grey dots). Non Gad2 putative pyramidal neuron doesn't express ChETA, thus exhibits only spontaneous spikes (yellow dots). b) The correspondent spike waveforms of Gad2 interneuron (light induced spikes in blue, and spontaneous spikes in grey; spike waveform similarity: r = 0.95) and putative non Gad2 pyramidal neuron (yellow). c) Summary of spike waveform similarity (r) of averaged light induced spikes and spontaneous spikes (top), and summary of light induced spike probability (bottom) throughout multiple stimulation frequencies (mean ± s.d., n=13, sorted neurons from 4 mice). d) Spike raster and peri-stimulus time histogram of Gad2 (left) and non Gad2 (left) neuron, with all spikes events aligned to light onset. Blue line indicates 1 ms light pulse. Only light tagged Gad2 interneuron exhibits low latency and high probability of light induced spikes. e) The correspondent cross-correlogram (CCG) between identified two neurons. Reference event: spikes from Gad2 interneuron (IN in red circle). Note strong and short-latency suppression of target spikes from non Gad2 pyramidal neuron (PN in white triangle), indicating the direct inhibitory interactions between neuron pairs.
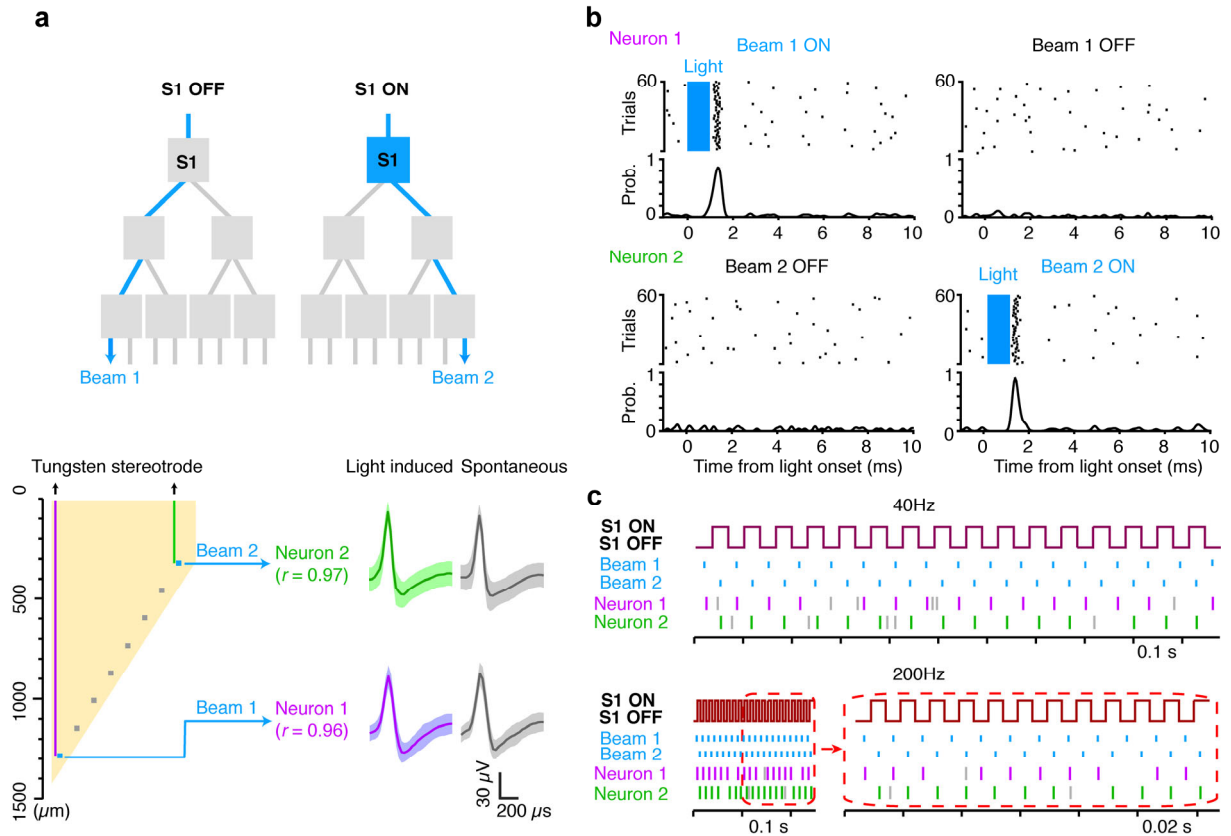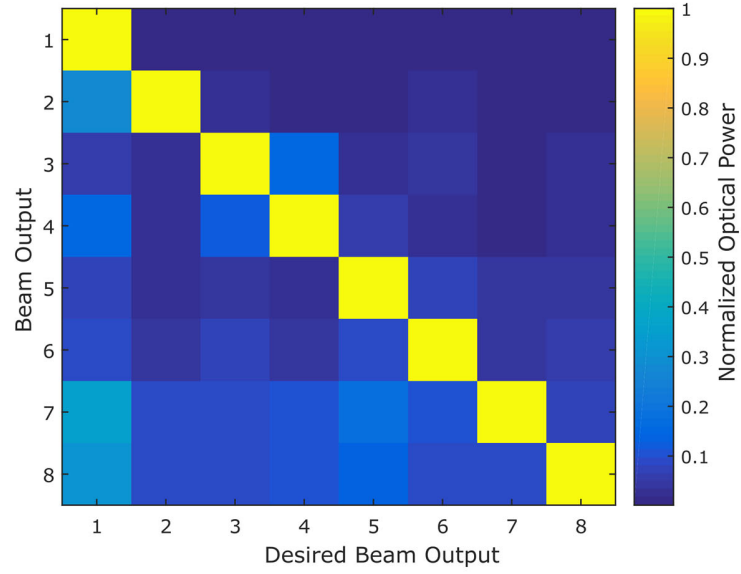
Supplementary Figure 6. In-vivo characterization of single switch performance (S1). a) Top: switch diagram shows how S1 state (OFF or ON) determines the beam direction (beam 1 or beam 2). Bottom: schematic of beam and electrode arrangement for in-vivo examination of effective optogenetic control of ChETA-expressing Gad2 interneuron's activity across visual cortex (V1) and hippocampus in anesthetized mice. Two tungsten stereotrodes (colored lines) are positioned next to beam 1 and 2 (blue squares separated in 875 μm in depth), respectively. The scale bar shown on the left indicates the insertion depth from brain surface. From each recording channel, single ChETA-expressing Gad2 interneuron (Neuron 1-2) is confirmed by evaluating the spike waveform similarity (r) of light induced spikes (averaged spike waveform in colored bold line, superimposed with color shaded s.d. of spikes) and spontaneous spikes (averaged spike waveform in grey bold line, superimposed with grey shaded s.d. of spikes). b) Representative spike raster and peri-stimulus time histogram of Neuron 1 and 2 when S1 is ON and OFF (Light pulse width: 1ms, blue line). c) Spike raster of Neuron 1 and 2 which follow the S1 OFF (beam 1 on) or S1 ON (beam 2 on) state with strong fidelity at both 40 Hz and 200 Hz. For each neuron, the colored line indicates light induced spike, and the grey line indicates spontaneous spike.
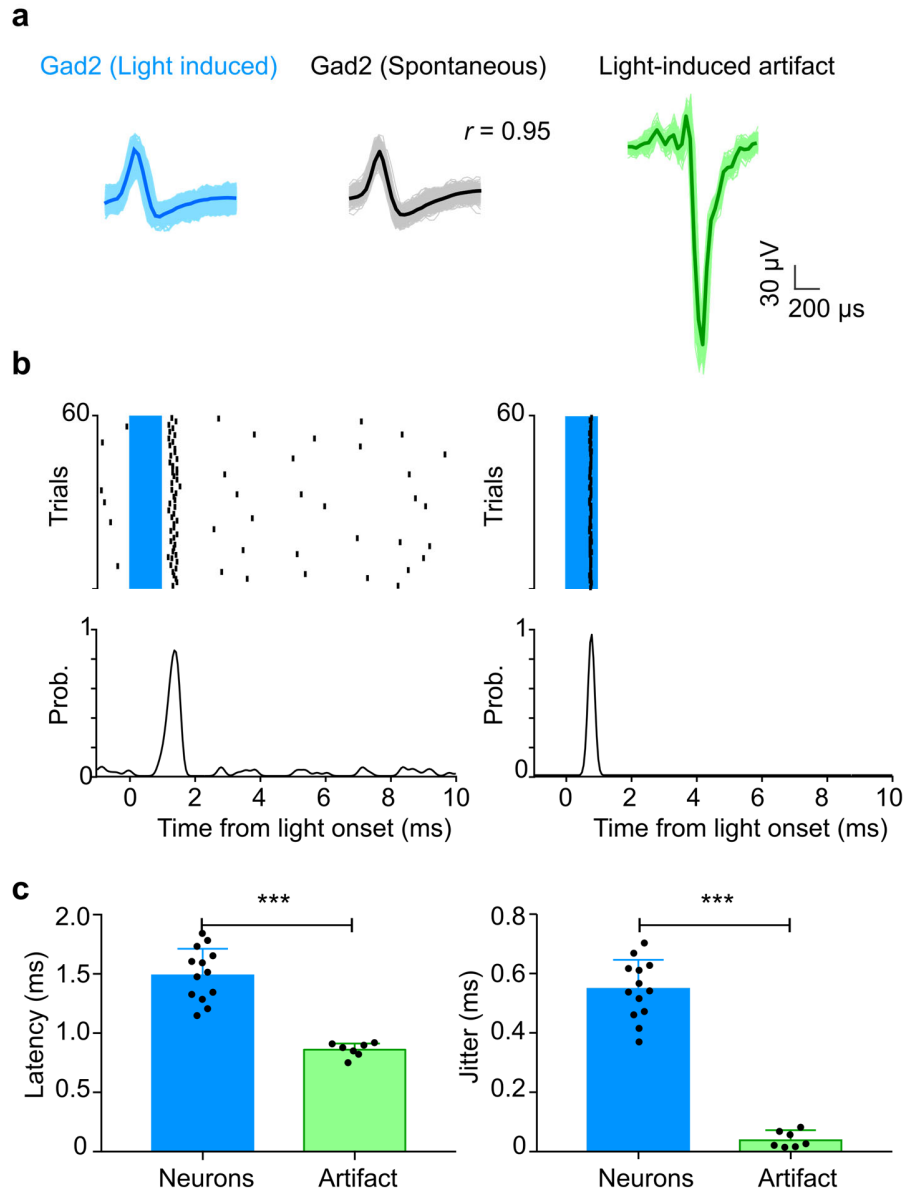
Supplementary Figure 7. Characterization of the difference in waveform and temporal response of light-induced spike and light-induced artifact. We eliminated the light-induced artifact that commonly occurs when light is incident on the exposed tungsten electrode tip. Here we show, how we can distinguish this waveform through spike-sorting to recover neural spike information. a) Left, example of spike waveform taken from ChETA-expressing Gad2 interneuron in **Supplementary Figure 5** (light induced spikes in blue, and spontaneous spikes in grey). The exposed tip of tungsten electrode is placed < 20 μm next to the emitter, presumably out of the cone of light; Right, example of robust and repeated light-induced artifact observed on tungsten electrode tip immersed in saline, which is directly exposure to the cone of light beam. No event matches with light-induced artifact's waveform when light is off. b) Raster plot and peri-stimulus time histogram of light-induced spikes and light-induced artifacts. Blue line indicates 1 ms light pulse and pulse onset is set to time '0'. c) Comparison of latency and jitter of the light induced spikes and artifacts. Optical artifact exhibits much shorter latency and much lower jitter than light-induced spike.
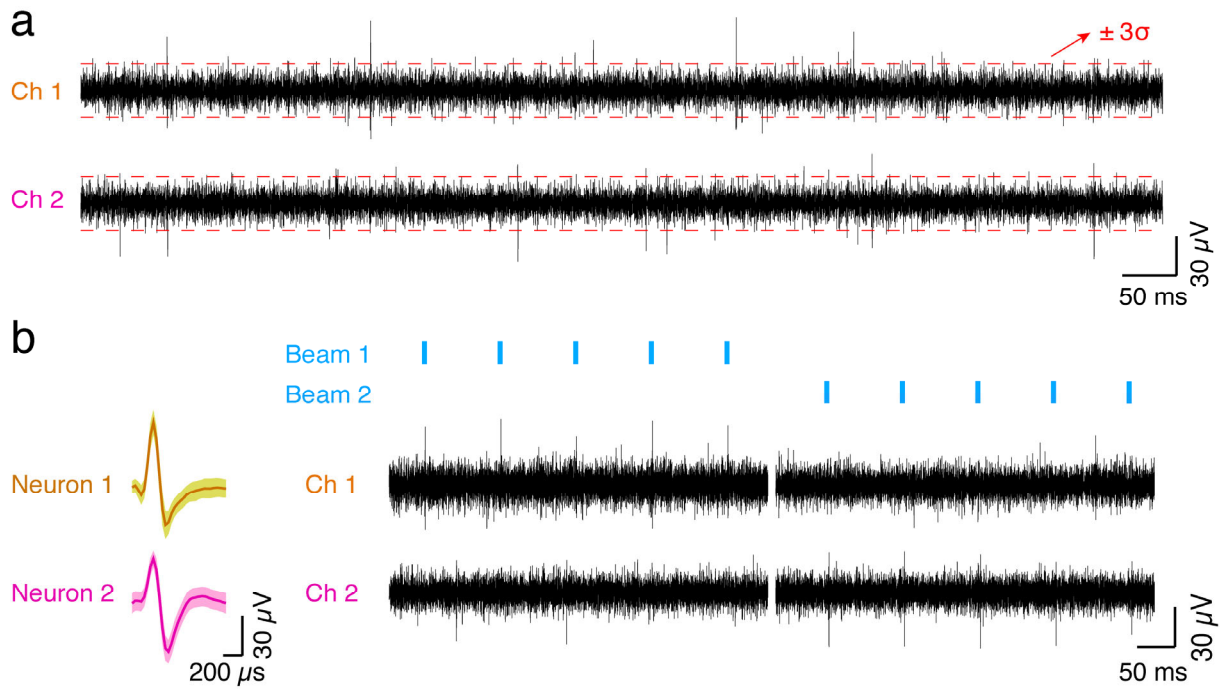
Supplementary Figure 8. Characterization of neural recording quality of the fully-integrated nanophotonic probe with Pt recording sites. a) Raw traces of spontaneous neural activities recorded from Ch 1 and Ch 2 of integrated nanophotonic probe shown in Fig. 5a. The quality of continuous electrical signal for each recording site is computed by measuring the peak to valley value of detected spikes relative to the standard deviation (σ) of the mean signal. The spike detection threshold is set as the ±3σ (standard deviation) of the mean signal. b) Left, spike template for Neuron 1 and 2 (averaged light induced spike waveform in colored bold line, superimposed with color shaded s.d. of spikes) recorded from Ch 1 and Ch 2, respectively. Right, continuous recording of individual light induced spikes from Ch 1 and Ch 2 when light is switched between beam 1 and beam 2.

12

Supplementary Figure 9. Optical crosstalk characterization of 8-beam nanophotonic probe. Plot shows the normalized beam output by measuring the optical power output from each grating emitter as each of the 8 beams is independently turned on (bottom = beam 1 and top = beam 8. While there is some small residual crosstalk for certain beam configurations due to fabrication imperfections, it did not limit our ability to individually route light through each emitter.
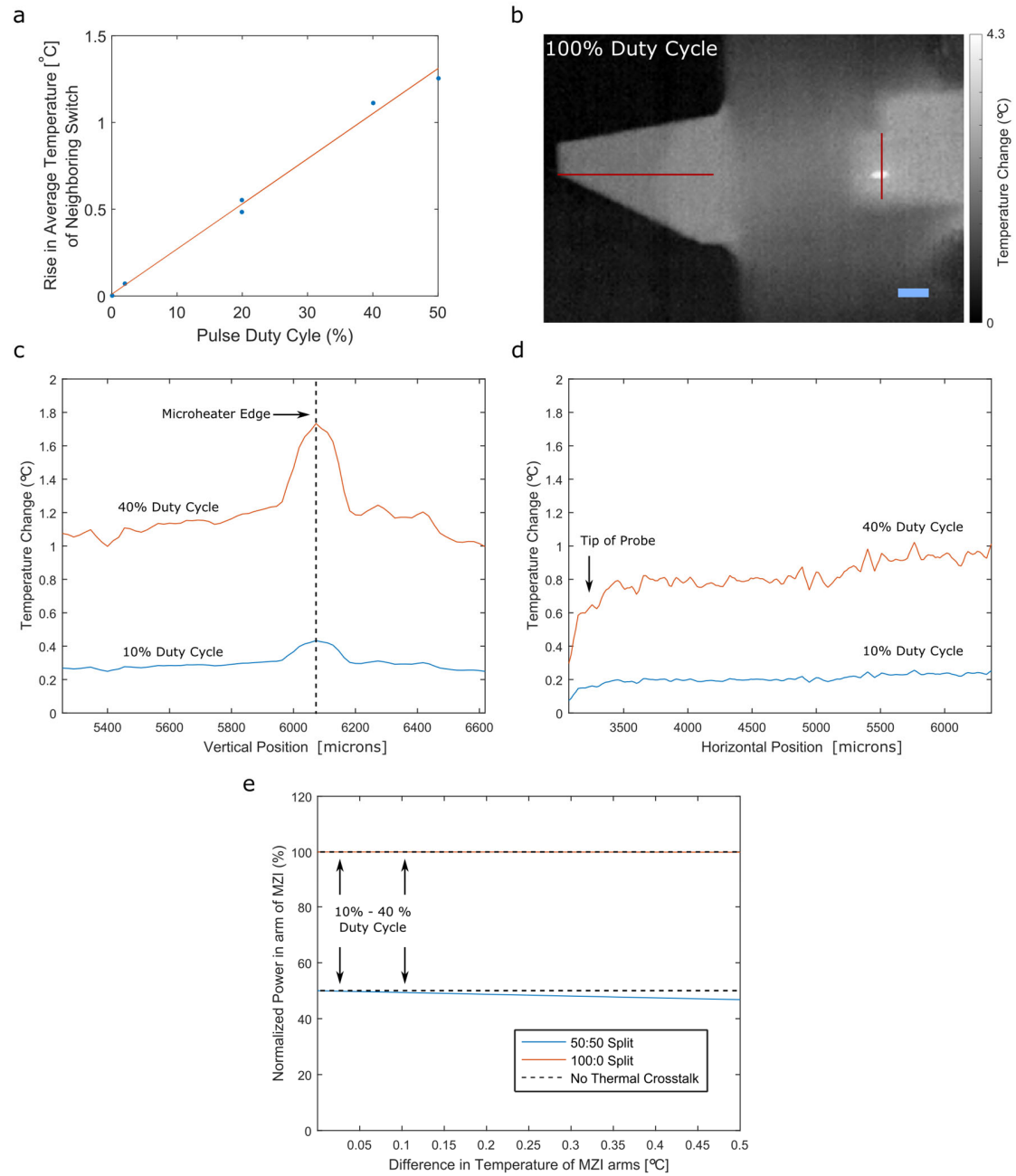
Supplementary Figure 10. Thermal crosstalk of the nanophotonic switch. a) Temperature measured at Switch 5 when Switch 4 (see diagram in Fig. 3a), about 200 μm away, is driven with power for pi-phase shift (30 mW) for pulse frequencies ranging from 1-200Hz for various duty cycles. The blue points represent temperature data derived from resistivity measurements based on a calibrated temperature coefficient of resistance of Pt. The orange line is a linear fit. b) Thermal image of the probe with S1 on with DC power on (100% duty cycle). The red lines indicate the vertical and horizontal slice of the data shown in parts c and d, respectively. Scale bar is 550 μm. c) Vertical slice of the temperature change distribution across microheater from part b for 40% and 10% duty cycle. Dashed line indicates center of microheater with 5 μm width. d) Horizontal slice of the temperature change distribution across the bottom tip of the probe from part b for 40% and 10% duty cycles. The peak in thermal image does not reflect the actual temperature at the 5 micron wide switch due to the resolution limitations of the thermal camera, which is about 30°C. e) Numerical calculation of the effect of temperature difference across MZI switch arms for the 100%:0% (full on state) and 50%:50% (half on state). Arrows indicate typical duty cycles for optogenetic experiments.
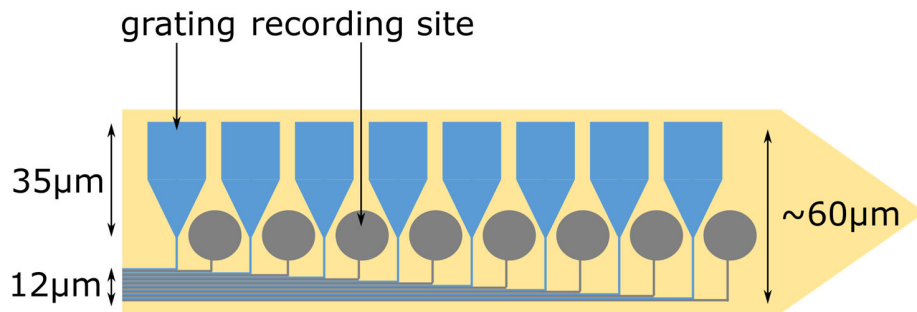
Supplementary Figure 11. Example of dense-packing of nanophotonic and recording electrode structures at tip of probe. Using the grating emitter design from Shim et al. and a waveguide spacing of 500 nm and waveguide width of 1 μm, the horizontal dimension of the probe can be reduced below 100 μm for up to 32. Note that when designing the probe architecture, since the electrical recording structures are fabricated on a separate layer above the cladding of the photonic structures one has the freedom to position the electrodes anywhere on the probe, including on an optical waveguide, except directly over the grating emitter.
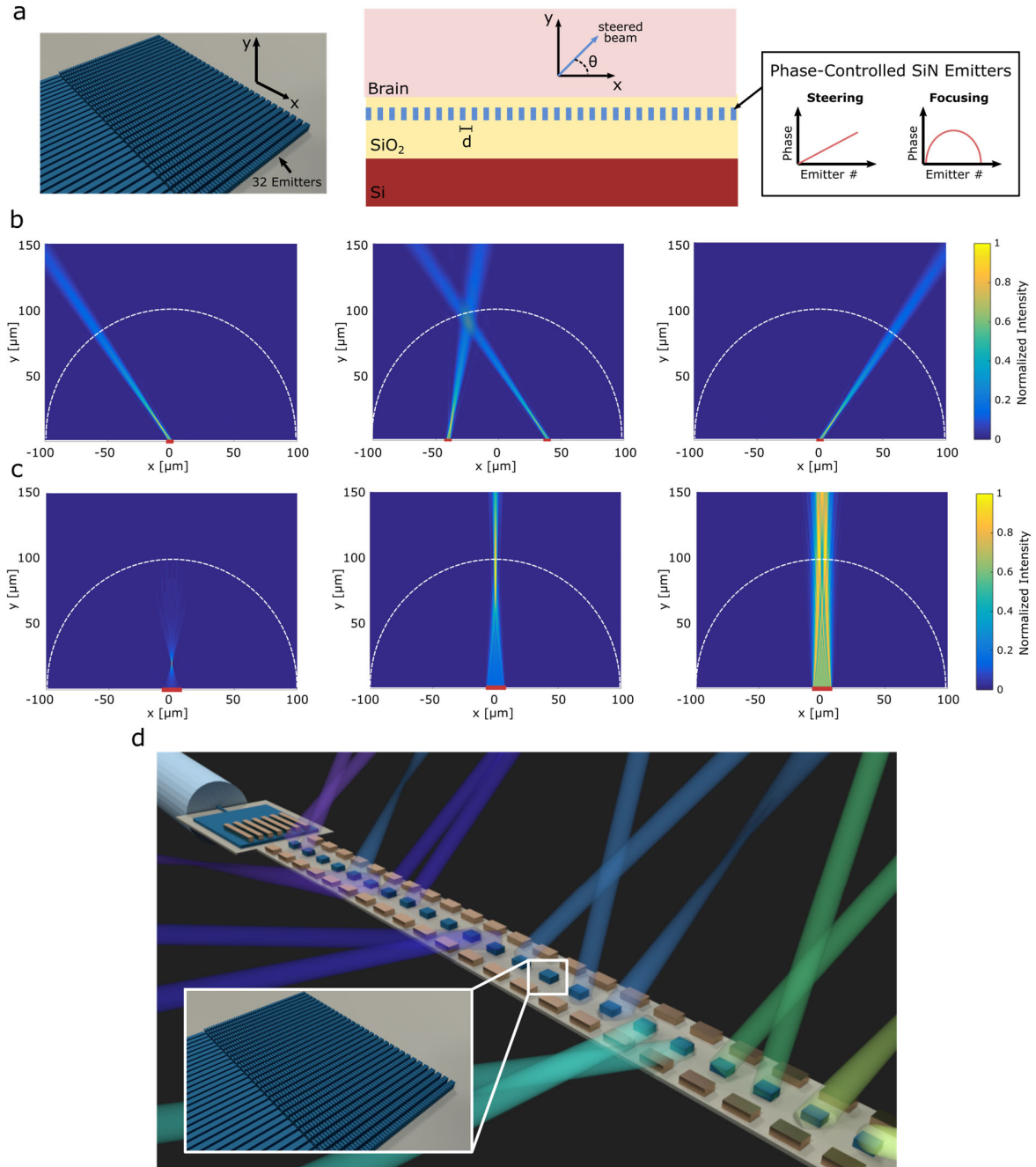
Supplementary Figure 12. Examples of beam shaping using nanophotonics. a) Left: Schematic of a tunable optical aperture made up of an array of 32 phase controlled emitters. Middle: Cross-section of structure shows direction of beam steering. Right: Examples of emitter phase profile for different functions (steering and focusing). b) Numerical simulation of steerable beams using a 32 emitter phased array with a linear phase profile and 100 nm spacing. The white hemisphere represents a radius of 100 μm where scattering effects become significant and recording electrodes lose sensitivity. For experiments without recording electrodes, different spacings, d, can be used to penetrate deeper. The number of elements can be reduced using a sparse aperiodic layout of emitters. c) Numerical simulation of focusing beams using a 32 emitter phased array with a quadratic phase profile and 480 nm spacing. d) Schematic of potential nanophotonic probe incorporating steerable and focused beams alongside recording electrodes.
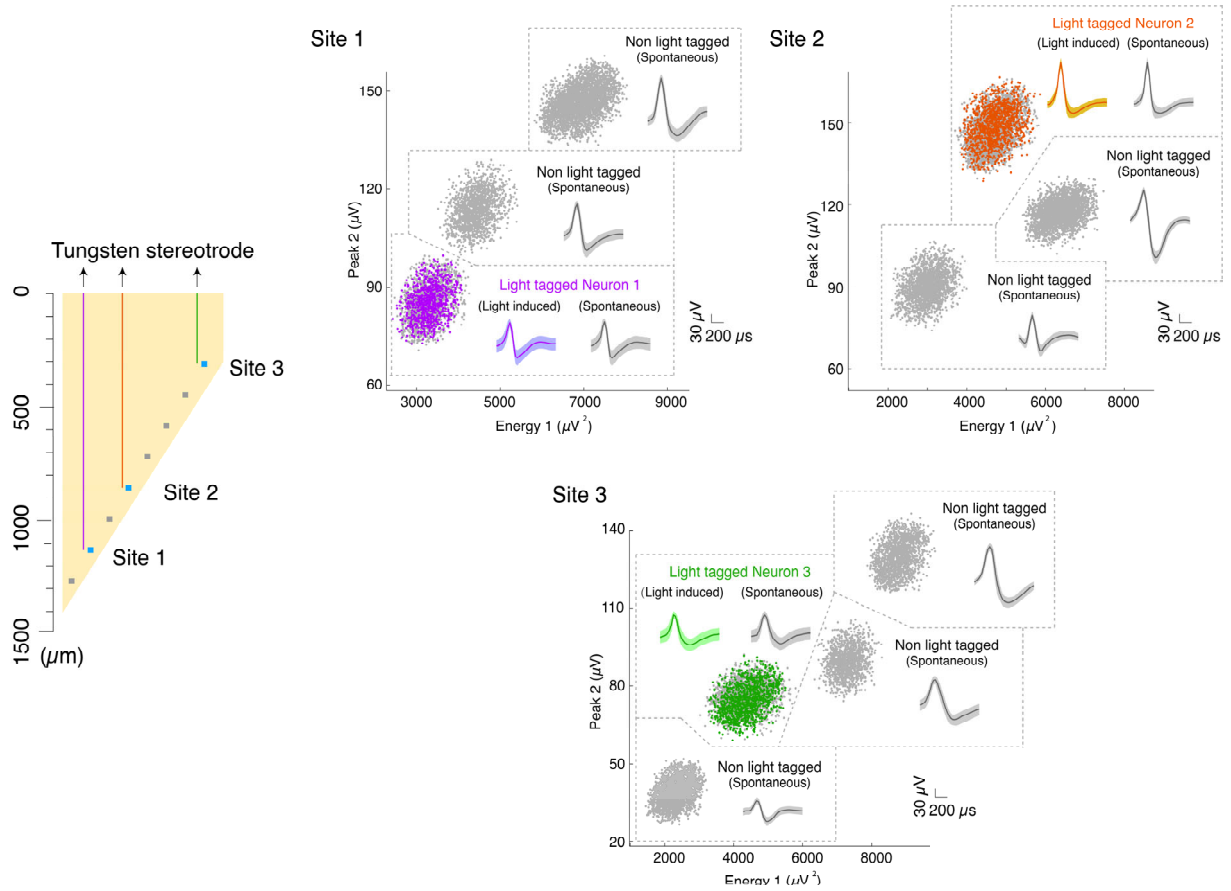
Supplementary Figure 13. Spike sorting examples from a single session shown in Figure 4. With stereotrode configuration, single neuron units were well isolated based on the spike waveform features shown in energy-peak space. 3 light tagged neurons (site1: purple; site2: orange, site3: green, same neuron as shown in Figure 4) were identified based on SALT optical tagging analysis, each showed light induced spikes (averaged spike waveform in colored bold line, superimposed with color shaded s.d. of spikes) overlaid with spontaneous spikes (averaged spike waveform in grey bold line, superimposed with grey shaded s.d. of spikes). Other non-light tagged neurons exhibited only spontaneous spikes (grey only).
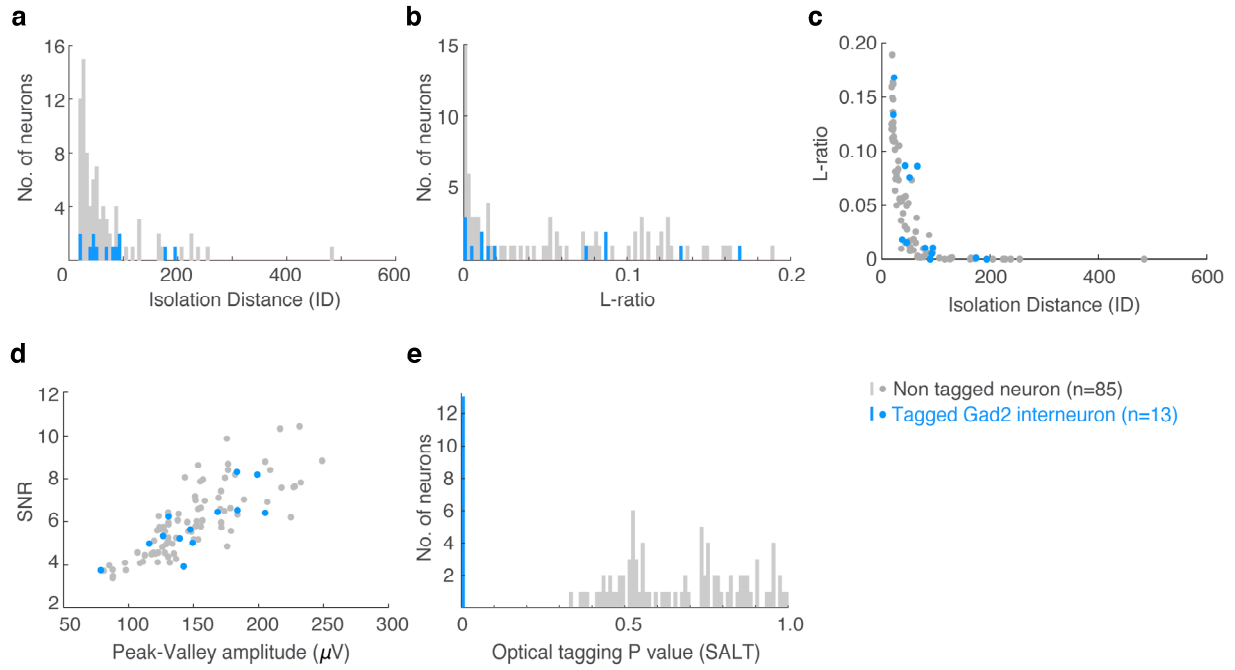
Supplementary Figure 14. Summary of single unit isolation quality using tungsten electrode. We used either stereotrodes (6 recording sessions) or sometimes single electrode configuration (4 recording sessions) to isolate single units and pooled the data for statistics analysis. a) Histogram of isolation distance (ID) and b), L-ratio for 13 light tagged Gad2 interneurons (blue) and 85 non-light tagged neurons (grey) from 10 recording sessions of 4 mice. The high value of ID (>18) and low value of L-ratio (<0.2) together indicate good cluster quality. c) Scatter plot of ID against L-ratio, reveals an inverse relationship. d) Scatter plot of spike peak-valley amplitude against SNR. e) Histogram of p value for SALT optical tagging analysis, which yields a bimodal distribution of p values. The yielded low p value (p<0.001) indicated significant light activation response (defined as light-tagged Gad2 interneurons in blue). The demonstrated light-tagged neurons (p value of SALT mean ± standard error: 0.000156 ± 0.00011, n=13 neurons in blue) are well separated from non-tagged neurons (p value of SALT mean ± standard error: 0.674 ± 0.020; n=85 neurons in grey).
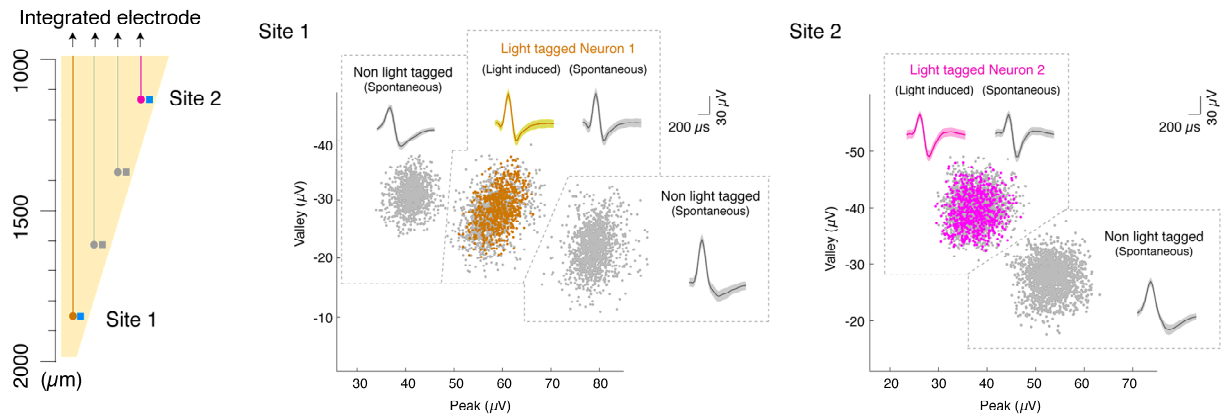
Supplementary Figure 15. Spike sorting examples from a single session shown in Figure 5. Single neuron units were well isolated based on the spike waveform feature shown in peak-valley space. 2 light tagged neurons (site1: orange; site2: pink, same neuron as shown in Figure 5) were identified based on SALT analysis, each showed light induced spikes (average spike waveform in colored bold line, superimposed color shaded s.d. of spikes) overlaid with spontaneous spikes (averaged spike waveform in grey bold line, superimposed grey shaded s.d. of spikes), and other non-light tagged neurons exhibited only spontaneous spikes (grey only).
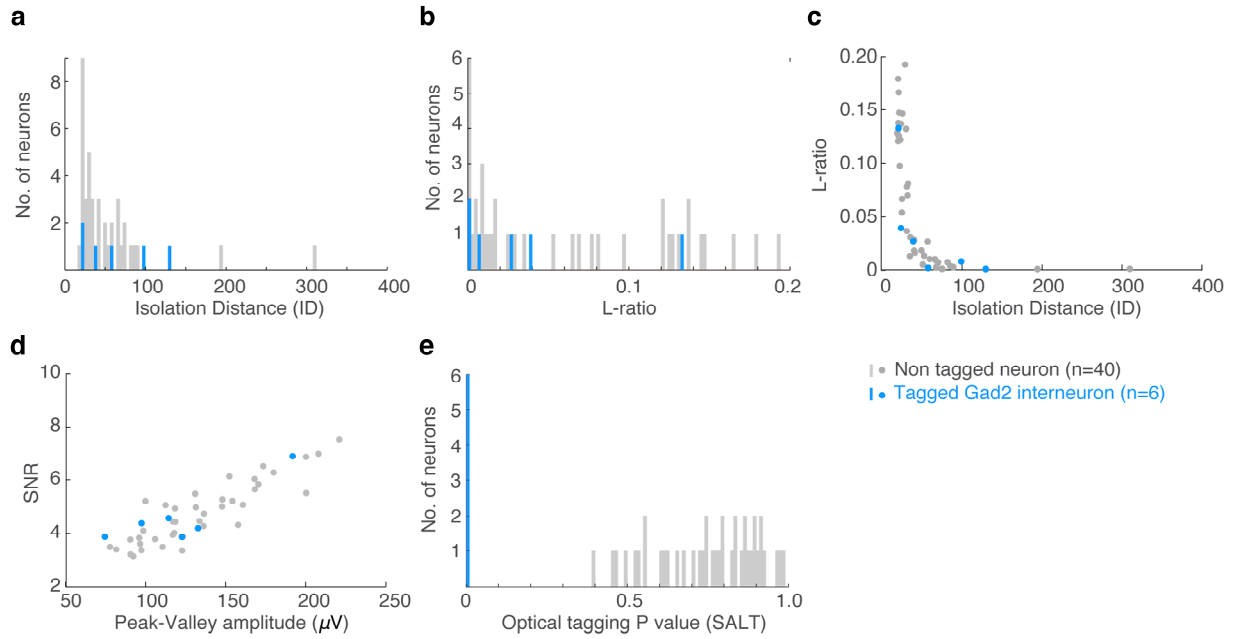
Supplementary Figure 16. Summary of single unit isolation quality using integrated probe. a) Histogram of isolation distance and b), L-ratio for 6 light tagged Gad2 interneurons (blue) and 40 non-light tagged neurons (grey) from 5 recording sessions of 3 mice. c) Scatter plot of ID against L-ratio. The high value of ID (>18) and low value of L-ratio (<0.2) together indicate good cluster quality. d) Scatter plot of spike peak-valley amplitude against SNR. e) Histogram of p value for optical tagging SALT analysis, which yields a bimodal distribution of p values. The yielded low p value (p<0.001) indicates significant light activation response (defined as light-tagged Gad2 interneurons in blue). The demonstrated light-tagged neurons (p value of SALT mean ± standard error: $6.84 \times 10^{-5} \pm 6.83 \times 10^{-5}$, n=6 neurons in blue) are well separated from non-tagged neurons (p value of SALT mean ± standard error: 0.748 ± 0.025; n=40 neurons in grey).

References:

1. Maese-Novo, A. *et al.* Wavelength independent multimode interference coupler. *Opt. Express, OE* **21**, 7033–7040 (2013).

2. Yang, Y. *et al.* Phase coherence length in silicon photonic platform. *Opt. Express, OE* **23**, 16890–16902 (2015).

3. Goh, T. *et al.* Low loss and high extinction ratio strictly nonblocking 16×16 thermooptic matrix switch on 6-in wafer using silica-based planar lightwave circuit technology. *Journal of Lightwave Technology* **19**, 371–379 (2001).

4. Marchetti, R., Lacava, C., Carroll, L., Gradkowski, K. & Minzioni, P. Coupling strategies for silicon photonics integrated chips [Invited]. *Photon. Res., PRJ* **7**, 201–239 (2019).

5. Cardenas, J. *et al.* High Coupling Efficiency Etched Facet Tapers in Silicon Waveguides. *IEEE Photonics Technology Letters* **26**, 2380–2382 (2014).

6. Khilo, A., Popović, M. A., Araghchini, M. & Kärtner, F. X. Efficient planar fiber-to-chip coupler based on two-stage adiabatic evolution. *Optics Express* **18**, 15790 (2010).

7. Roelkens, G., Van Thourhout, D. & Baets, R. High efficiency Silicon-on-Insulator grating coupler based on a poly-Silicon overlay. *Optics Express* **14**, 11622 (2006).

8. Shim, E., Chen, Y., Masmanidis, S. & Li, M. Multisite silicon neural probes with integrated silicon nitride waveguides and gratings for optogenetic applications. *Scientific Reports* **6**, 22693 (2016).

9. Hoffman, L. *et al.* Low Loss CMOS-Compatible PECVD Silicon Nitride Waveguides and Grating Couplers for Blue Light Optogenetic Applications. *IEEE Photonics Journal* **8**, 1–11 (2016).

10. Ji, X. *et al.* Ultra-low-loss on-chip resonators with sub-milliwatt parametric oscillation threshold. *Optica* **4**, 619 (2017).

11. Kiyatkin, E. A. & Brown, P. L. Modulation of physiological brain hyperthermia by environmental temperature and impaired blood outflow in rats. *Physiol. Behav.* **83**, 467–474 (2004).

12. Murray, K., Lu, Z., Jayatilleka, H. & Chrostowski, L. Dense dissimilar waveguide routing for highly efficient thermo-optic switches on silicon. *Optics Express* **23**, 19575 (2015).

13. Liang, G. *et al.* Micron-scale, Efficient, Robust Phase Modulators in the Visible. in *Conference on Lasers and Electro-Optics (2019), paper JTh5B.4* JTh5B.4 (Optical Society of America, 2019). doi:10.1364/CLEO_AT.2019.JTh5B.4

14. Segev, E. *et al.* Patterned photostimulation via visible-wavelength photonic probes for deep brain optogenetics. *Neurophotonics* **4**, 011002 (2016).

15. Pisanello, F. *et al.* Multipoint-Emitting Optical Fibers for Spatially Addressable In Vivo Optogenetics. *Neuron* **82**, 1245–1254 (2014).

16. Pisanello, F. *et al.* Dynamic illumination of spatially restricted or large brain volumes via a single tapered optical fiber. *Nature Neuroscience* **20**, 1180–1188 (2017).

17. Wu, F. *et al.* Monolithically Integrated μLEDs on Silicon Neural Probes for High-Resolution Optogenetic Studies in Behaving Animals. *Neuron* **88**, 1136–1148 (2015).

18. Kim, T. -i. *et al.* Injectable, Cellular-Scale Optoelectronics with Applications for Wireless Optogenetics. *Science* **340**, 211–216 (2013).